Scripta Materialia 178 (2020) 62–66

Contents lists available at ScienceDirect

Scripta Materialia

journal homepage: www.elsevier.com/locate/scriptamat

Highly mobile twin boundaries in seven-layer modulated Ni–Mn–Ga–Fe martensite

Alexei Sozinov[a,*], Denys Musiienko[a,b], Andrey Saren[a], Petr Veřtát[b], Ladislav Straka[b,c], Oleg Heczko[b,c], Martin Zelený[c,d], Robert Chulist[e], Kari Ullakko[a]

[a] Material Physics Laboratory, LUT University, Lappeenranta 53850, Finland
[b] Institute of Physics, Czech Academy of Sciences, Prague 18221, Czech Republic
[c] Faculty of Mathematics and Physics, Charles University, Prague CZ-12116, Czech Republic
[d] Faculty of Mechanical Engineering, Institute of Materials Science and Engineering, Brno University of Technology, Brno CZ-61669, Czech Republic
[e] Institute of Metallurgy and Materials Science, Polish Academy of Sciences, Krakow 30-059, Poland

ARTICLE INFO

Article history:
Received 4 September 2019
Revised 24 October 2019
Accepted 26 October 2019
Available online 13 November 2019

Keywords:
Magnetic shape memory
Martensite
Twin boundary
Ni–Mn–Ga
Heusler alloy

ABSTRACT

We report on low twinning stress of 0.2 MPa for type 1 twin boundaries with rational (101) twinning plane and 0.1 MPa for type 2 twin boundaries with rational [$\bar{1}$01] twinning direction, in $Ni_2MnGa_{0.8}Fe_{0.2}$ seven-layer modulated martensite exhibiting about 12% stress-induced strain. The studied samples were free of compound twins with (100) and (110) twinning planes. The martensite lattice is monoclinic and shows a long-period commensurate modulation with wave vector $\boldsymbol{q}=(2/7)\boldsymbol{g}_{\mathbf{110}}$, where $\boldsymbol{g}_{\mathbf{110}}$ is the reciprocal lattice vector. The investigated alloy has high potential for practical applications due to the low twinning stress and the elevated Curie point T_C=400 K.

The ability of crystals to create twins was recognized long ago [1]. Twins are often observed in different processes such as solidification, recrystallization, deformation, and solid-state phase transformations in a variety of crystalline solids. Twins occur on the nanometer-to-millimeter scale and usually have lower interface energy levels than general grain boundaries. Next only to grain boundaries, twin boundaries have emerged as the second most significant interface in materials science. The key role of twinning has been proved in recently developed nanotwinned materials – in ultrafine-grained metals with nanotwinned structure [2], in cubic face-centered alloys ductile at low temperatures [3], in ferroelastic materials [4], in shape memory materials [5], and in magnetic shape memory (MSM) materials [6]. Each group of materials takes advantage of twin boundary properties that are essentially different.

MSM materials capable of generating motion and force in an applied magnetic field require twin boundaries (TBs) with high mobility. The twinning stress (TS) in MSM materials should be lower than the magnetic stress [7] associated with high magnetic anisotropy of low symmetry martensite lattice, which is of the order of a few MPa [6]. It is not yet clear how to design new MSM materials with low TS and what the atomic mechanisms of TB motion in those materials should be. The Ni–Mn–Ga-based system exhibits magnetically-induced reorientation (MIR) or the MSM effect in all three of its most common martensitic phases: five-layer modulated (10M), seven-layer modulated (14M) and nonmodulated (NM) tetragonal martensites with magnetic field-induced strains of up to 12% [6,8]. No other material showed a giant MSM effect in the three different martensites of the same system, justifying a strong focus on this particular example. Recent investigations have revealed significant differences in TS [9–12] and TB kinetics [13] in 10M $Ni_{50}Mn_{25+x}Ga_{25-x}$ martensites for type I and type II TBs. The strong increase in TS for type I *a/c* TBs with lower temperatures, together with the unresolved problem of creating a fine twin microstructure consisting of type II TBs with low TS at a wide temperature range, may limit the use of 10M Ni–Mn–Ga martensite, despite the highest magnetic stress in 10M compared to 14M and NM martensites [6]. In an attempt to overcome these 10M martensite limitations, in the current investigation, we study $Ni_{50}Mn_{25}Ga_{20}Fe_5$ 14M modulated martensite – for which the mobility of type I and type II *a/c* TB is unreported. To confirm that this is the right direction, we draw upon the latest investigation of 14M martensite in $Ni_{50.5}Mn_{28.9}Ga_{20.6}$, with room temperature measurement of TS σ_{TW}=0.64 MPa [14], which proved that it is appropriate for actuator applications. Unfortunately, the TB type was not distinguished by this investigation.

* Corresponding author.
E-mail address: asozinov.fin@gmail.com (A. Sozinov).

https://doi.org/10.1016/j.scriptamat.2019.10.042

Table 1
The lattice parameters of the studied alloy in the cubic coordinate system, conventional monoclinic and in the conventional long-period monoclinic coordinate system, marked as LP.

Cubic	*a*, Å	*b*, Å	*c*, Å	*γ*, *deg.*	*V*, Å^3
	6.194	5.780	5.499	90.55	196.87
Monoclinic	a_m	b_m	c_m	β_m	V_m
	4.256	5.499	4.216	93.96	98.43
LP	a_{LP}	b_{LP}	c_{LP}	β_{LP}	V_{LP}
	4.256	5.499	29.510	93.96	689.04

We show in the present paper that the $Ni_{50}Mn_{25}Ga_{20}Fe_5$ alloy with a relatively high Curie point of T_C=400 K yields a low twinning stress of 0.2 and 0.1 MPa, respectively, for type I and type II TBs at ambient temperature. We argue that the influence of composition and temperature on TB mobility in martensites with 14M crystal structure should be subject to further study due to the high potential for practical MSM applications and a better understanding of TB behavior.

Initially, we scanned the composition range $Ni_{50}Mn_{25}Ga_{25-x}Fe_x$ (x = 0–5.5%), which is interesting for practical applications because, according to previous investigations, replacing Ga with Fe atoms increases Curie point as well as martensite transformation temperatures [15–17]. Among the studied alloys, we selected $Ni_{50}Mn_{25}Ga_{20}Fe_5$ composition with 14M modulated martensite at ambient temperature. Compositions with less iron content $Ni_{50}Mn_{25}Ga_{20.5}Fe_{4.5}$ are a mixture of 10M/14M martensites, while compositions with less than 4% iron content are 10M martensite. Adaptamat Ltd has grown and heat-treated the single-crystal bar with nominal composition $Ni_{50}Mn_{25}Ga_{20}Fe_5$. A few specimens with the size of 10 × 2.5 × 1.5 mm^3 were cut from the bar in the austenite state along (100) crystallographic planes, then ground and electro-polished. The martensite transformation temperatures and the Curie point were determined from low-field *ac* magnetic susceptibility temperature dependencies, measured with home-built apparatus. The specimens exhibited martensitic transformation at $T_M = (M_s+M_f)/2$ = 329 K, and reverse transformation at $T_A = (A_s+A_f)/2$ = 332 K, ($M_s - M_f$)=(A_f-A_s)=3 K, where M_f, M_s, A_s, A_f are martensite and austenite start and finish temperatures. Temperatures of intermartensitic transformation were $T^{7M\text{-}NM}$ =218 K and reverse $T^{NM\text{-}7M}$ =285 K. We found some peculiarities a few degrees below T_A in the magnetic susceptibility curves that are likely to show a transition of 10M–14M and will be studied more closely and reported separately. As per previous studies [15–17], T_C = 400 K is greater than measured for Ni–Mn–Ga alloys, where T_C < 380 K [18,19]. It is important to note that the iron atoms in the Heusler-type alloy $Ni_{50}Mn_{25}Ga_{20}Fe_5$ do not occupy deficit gallium places. Detailed analysis [20,21] revealed that iron prefers the regular manganese sites with a ferromagnetic exchange. The excess and displaced manganese occupy the vacant gallium sites with an antiferromagnetic exchange.

The formation of a single-variant state (SVS) in the 14M martensite was accomplished by compressing of multivariant samples in different directions at temperatures 5÷10° below the reverse martensite-austenite transformation temperature, T_A. This method has already been used and explained in detail in a previous investigation [22]. A PANalytical Empyrean X-ray diffractometer equipped with Co tube, hybrid monochromator, Eulerian cradle, and a Pixel3D detector was used for the lattice parameters measurement, allowing for determination of the domain orientation, reciprocal space mapping and the conducting of Q-scans along different reciprocal space lines.

We recorded diffraction peaks from different sides of the SVS samples to determine the lattice parameters shown in Table 1. The parameters – referred to as cubic system – describe the martensite lattice as a distorted $L2_1$ cubic lattice [23–25]. The parameters, which are referred to as a conventional monoclinic system, describe the martensite lattice using c_m-axis parallel to [110], a_m-axis parallel to [$\bar{1}$10], and b_m-axis parallel to the *c*-axis of the cubic system [26–28]. The main diffraction peaks only were used to calculate the parameters in cubic or conventional monoclinic coordinates and the satellite peaks were disregarded. Such a procedure provides the *average lattice* parameters of complex modulated structures that are either commensurate or incommensurate [29,30]. All peaks were taken into account for conventional monoclinic long-period (LP) lattice, also presented in Table 1. We used the lattice parameters in cubic coordinates to describe experimental data and to calculate the twinning elements.

The samples were free of *a*/*b* and modulation twins, with corresponding twinning planes (110) and (100). Fig. 1a shows the distribution of X-ray intensity for a single variant $Ni_{50}Mn_{25}Ga_{20}Fe_5$ 14M martensite sample collected by Q-scan in the a^*–b^* plane along the line parallel to [110]* and crossing basic peaks (040) and (260), where * marks the reciprocal lattice. The satellite peaks S_j^{hkl} are distinguished by the indexes closest to the main peak (hkl) and by the satellite order +*j* or –j indicating the positions of the satellite peaks relative to the main peak (hkl), in respect of the directions [110]* or -[110]*. The six satellite peaks are equally distant between the main peaks (040) and (260) and show the commensurate modulation of the seven-layer lattice. Comparing the distance |*q*| between the nearest satellite peaks in reciprocal space along [110]* with the distance $|\boldsymbol{g_{220}}|=2|\boldsymbol{g_{110}}|=2|\boldsymbol{c_m^*}|$ between basic (040) and (260) peaks, we conclude that the modulation wave vector $\boldsymbol{q}=(2/7)\boldsymbol{g_{110}}=(2/7)\boldsymbol{c_m^*}$ is commensurate to the reciprocal vector $\boldsymbol{g_{110}}$ in cubic or to $\boldsymbol{c_m^*}$ vector in a monoclinic coordinate system. This is different from other authors [26–28,31–36] who used polycrystalline and multivariant Ni–Mn–Ga specimens. They reported modulation vector $\boldsymbol{q}=(0.430\pm0.003)\boldsymbol{c_m^*}$ for Ni_2MnGa [33–36], and $\boldsymbol{q}=(0.307\pm0.001)\boldsymbol{c_m^*}$ for nonstoichiometric Ni–Mn–Ga alloys [26–28,31,32]. The sample preparation method, the single variant state or the composition of the alloy may be responsible for the commensurate modulation in our samples. The rational value of the $\boldsymbol{q}$ found in the $Ni_{50}Mn_{25}Ga_{20}Fe_5$ alloy is expected by the nanotwin model for the 14M modulated martensite crystal structure [37,38]. However, in order to prove the model, the intensity of the diffraction peaks should be analyzed to find atomic coordinates as it was made in Ref. [39] for the $Ni_2Mn_{1.4}In_{0.6}$ alloy. Fig. 1b shows that the SVS sample nearly has one direction of modulation [110]*. Small intensity satellite peaks along [$\bar{1}$10]*, noticeable in a logarithmic intensity scale of the reciprocal a^*–b^* map, show that the sample has less than 0.1% of the second modulation variant.

In magnetic field $\mu_0 H$ = 0.2 T or under small compressive stress, the SVS sample showed a reorientation strain of around 12%, which was expected by crystallography in cubic coordinates for *a*–*c* axes reorientation. Two different types of highly mobile TBs with non-segmented straight traces were observed during the sample reorientation. To reveal the nature of such TBs in 14M martensite, we used a specific twin variant configuration consisting of three domains, as shown in Fig. 2a. The domains *D1* and *D2* were created from *D0* by field-induced reorientation of a partially constrained SVS sample. Using X-ray diffraction, we found that the b^*-axes of *D0, D1*, and *D2* domains have approximately the same orientation, whereas modulation directions [110]* in *D1* and *D2* deviate by about 90° from each other (orientation comparison is shown by green arrows and lines in Fig. 2a and b). This clearly indicates a different symmetry element connecting *D0* and *D1* in comparison with *D0* and *D2*. By comparing the orientations of *D0* and *D1*, we concluded that the twinning plane between *D0* and *D1* is a mirror plane corresponding to type I TB. Also, using the measured lattice parameters and the arguments and equations presented in reference [10], we found that a type II irrational twinning plane deviates from type I TB by rotation around the [101] axis by 3.44°.

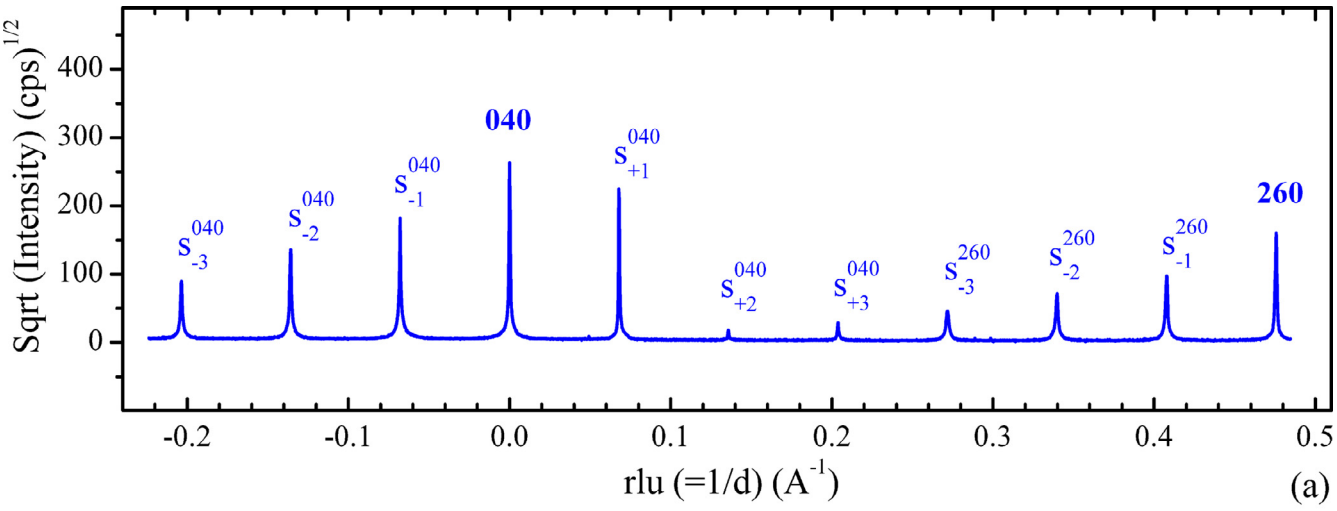

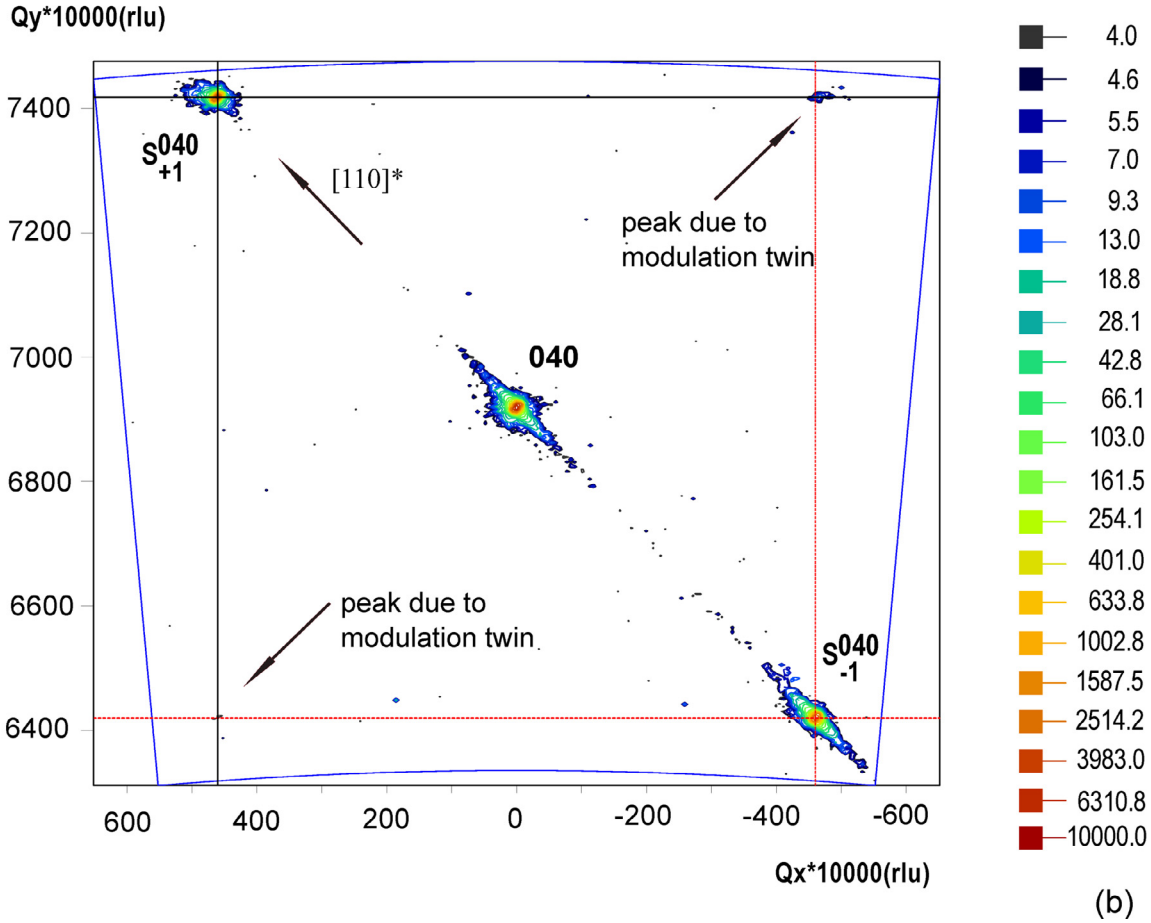

Fig. 1. (a) X-ray intensity distribution for single variant $Ni_{50}Mn_{25}Ga_{20}Fe_5$ 14M martensite recorded by Q-scan in the a^*–b^* plane along the line [110]* and crosses over main peaks (040) and (260). The equally distant satellite peaks $S_j^{(hkl)}$ manifest the 7-fold commensurate lattice modulation. The satellite peaks are distinguished by the indexes closest to the main peak (hkl) and by satellite order $+j$ or $-j$, which indicates the position of the satellite peaks relative to the main peak (hkl), along [110]* or -[110]* directions correspondingly.
(b) Reciprocal map of diffraction intensities presented in logarithmic scale near the main peak (040) in the plane (hk0)* showing high-intensity satellites $S_1^{(040)}$ and $S_{-1}^{(040)}$ along [110]*, while the intensity of the satellites in $[\bar{1}10]^*$ direction is close to the background level. The satellite peak located along the line parallel to $[\bar{1}10]^*$ direction is due to the modulation twin (see definition of the modulation twin in [9]). The ration of the satellite peak intensities in $[\bar{1}10]^*$ direction to the intensities in [110]* direction is below 10^{-3}, indicating that the sample has nearly one modulation domain.

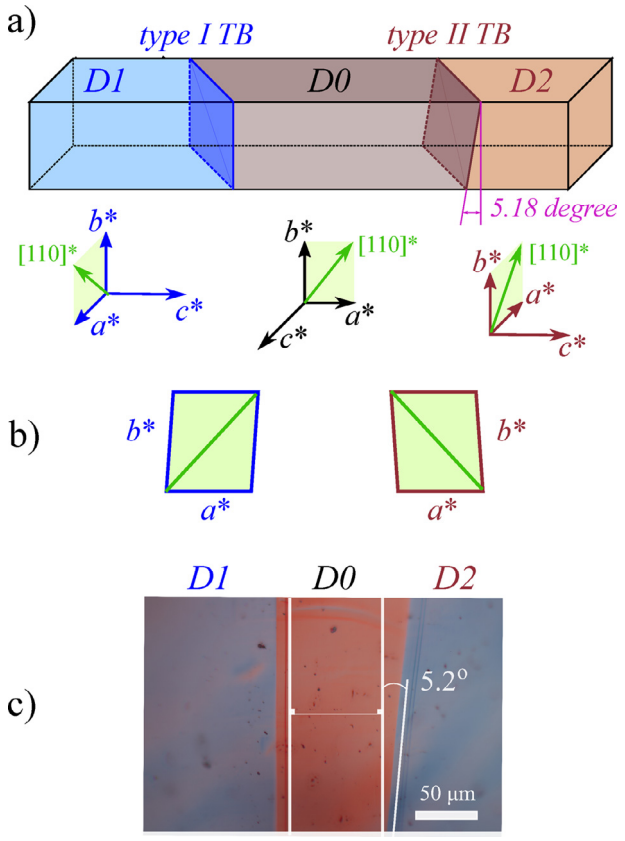

Fig. 2. (a) Schematic view of the studied $Ni_{50}Mn_{25}Ga_{20}Fe_5$ 14M martensite sample consisting of three crystallographic domains: matrix *D0*, type I twin *D1*, type II twin *D2*. The vectors of the reciprocal space a^*, b^* and c^* show orientation of the domains. [110]* is the direction of lattice modulation. Type I twin boundary (TB) is the crystallographic plane (101). The calculated angle between traces of TB planes type I and type II on the front sample surface is equal to 5.18°. (b) A view of the lattices *D1* and *D2* along c^*-axis showing the different orientation of the directions of modulation [110]* marked by green lines. (c) Optical image of the front sample surface with type I and type II TBs in close proximity. The sample was compressed along c^*-axes of *D1* and *D2* domains to reduce the distance between the TBs. The Zeiss Axio Scope.A1 microscope and differential interference contrast (DIC) were used to record the image. The measured angle between the traces of type I and type II TBs is $5.2 \pm 0.2°$.

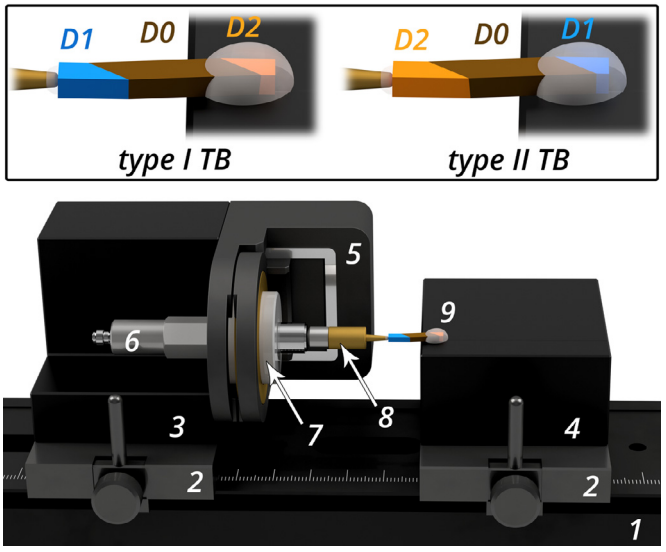

Fig. 3. 3D rendering of the in-house built machine for stress-strain measurements and specimen emplacement for twinning stress measurements of twin boundaries of type I and type II (inset). The setup consists of an optical rail (1), two coarse positioning stages (2), custom mounts (3, 4), a piezo positioning system (5), a force sensor (6) with mounting adapter (7), a brass pushing rod (8) and a measured sample (9) glued to the pushing rod (8) and to the upper surface of the mount (4). The inset shows how the TB of one type was constrained by the glue while the TB of the other remained movable.

Furthermore, the angle between traces of TB planes type I and type II on the front sample surface should be equal to 5.18°, see Fig. 2a. This value is in excellent agreement with the experimentally measured value of $5.2 \pm 0.2°$ between two traces of twinning planes *D1/D0* and *D0/D2* projected on the front surface, as per Fig. 2c. Orientations of the domain *D0* and *D2* are equated with a rotation of 180° around the axis [101]. Therefore, we have strong arguments that domains *D1* and *D2* are type I and type II twins, respectively, to the matrix domain *D0*. Using texture-type X-ray scans for all domains *D0, D1*, and *D2* (see Fig. 2a), we found no a^*-axis near b^*-axis. This observation, together with the 12% percent strain observed in the sample during its full magnetic field reorientation, provides a strong confirmation of the absence of *a/b* TBs in the sample.

Measurements of twinning stress were carried out using the in-house built stress-strain machine shown in Fig. 3. The PI, PIFOC PD72Z4CAQ, with a controller E-709 operated in closed-loop mode, provided strain control precision and force application. Kistler, Type 9207 with a controller Type 5867B was used to measure the force applied to the sample with ~50 μN accuracy in the range from −5 to 5 N. The force sensor is measuring the change of a charge on a piezo crystal, which is converted to the change of the axial force according to the factory calibration curve. The sample was glued to the stage on one side and the pusher rod was glued to the free end of the sample (see insert in Fig. 3). Such a sample attachment enables one TB to be constrained and the second to be mobile in a particular experiment. Since the zero-force level cannot be defined in our system, we conducted a tensile-compressive cycle loading for each type of TB. To avoid the bending of the sample, which can affect the stress-strain curve, the small TB displacement of ±200 μm was selected. The distance between compression and tensile parts of the curve was taken as double value of TS (Fig. 4) and averaged along the curve.

Fig. 4 shows the results of the TS measurements for both types of TBs in the $Ni_{50}Mn_{25}Ga_{20}Fe_5$ 14M martensite. The twinning stress is very low for both types of TBs, being 0.2 MPa for type I TB and 0.1 MPa for type II TB. Thus, TS of type I TB is quite close to TS of type II TB, as opposed to 10M martensite, where 20–30° below T_A, TS of type I and TS of type II TB are ten times different [9–11]. This result supports the model suggested by Seiner et al. [40] that *a/b* laminate, which plays a major role in increasing type I TB twinning stress in 10M martensite, cannot increase type I TB TS in 14M martensite owing to the absence of such lamination. The recently suggested model for TS in 10M Ni–Mn–Ga martensite [41] does not recognize *a/b* twin domains as a major factor for TS and predicts a huge difference of a factor of 40 in TS for type I and type II TB, which is not the case in 14M martensite. Other models [42–44] substantially overestimate the level of TS in 14M martensite. This implies that atomic-level TB structure studies are needed to understand the difference in TB mobility between type I and type II TBs in 14M and 10M martensites.

In the case of Ni–Mn–Ga 10M martensite, there is a qualitatively large difference in TS temperature dependencies for type I and type II TB [11,12]. These dependencies have not yet been determined in 14M martensite. Nevertheless, we can now already make preliminary estimations of the TS temperature dependence slope for type I TB. Based on the measured value of the TS, σ_{TW} =0.2 MPa at T = 298 K and expected $\sigma_{TW} > 0$ at $T = T_A = 332$ K, the maximal absolute value of the slope is below 0.006 MPa/K. Comparing the slope of 0.006 MPa/K for the 14M

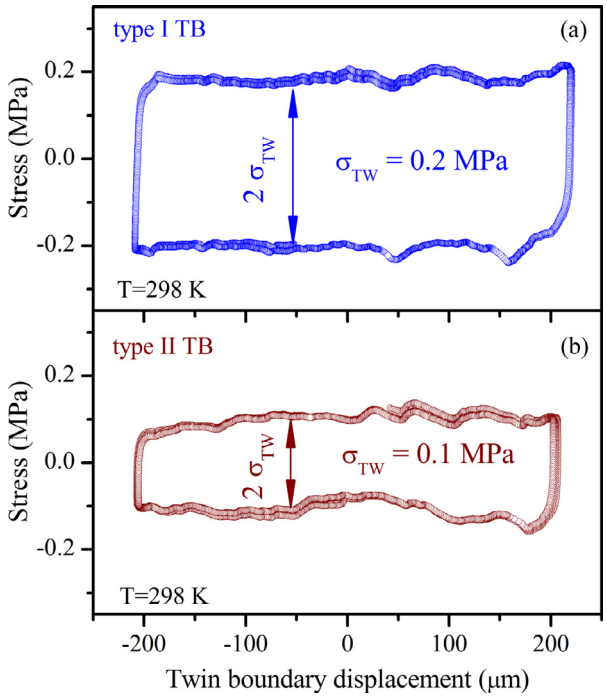

Fig. 4. Tensile – compression cycles measured for single-crystalline $Ni_{50}Mn_{25}Ga_{20}Fe_5$ 14M martensite, for single twin boundary of type I (a) and type II (b). Average twinning stress σ_{TW} is marked in figure.

martensite with the slope of 0.04 MPa measured for type I TBs in 10M $Ni_{50}Mn_{25+x}Ga_{25-x}$ martensite [11], we note that the temperature influence on TS in the studied 14M martensite is 6.7 times lower than in 10M martensite. This means that, compared to 10M martensite, 14M martensite possessing low TS type I TBs can be used in a significantly broad temperature range actuation. In fact, creating a fine twin microstructure in 10M martensite consisting of type II TBs that are preferable for practical applications is a complicated challenge that remains unresolved. Whereas creating such a microstructure composed of Type I TBs appears much easier [45,46]. We believe that the 14M martensite in actuator applications becomes a strong competitor of the 10M martensite due to weaker temperature dependence and low TS level for type I TBs.

In conclusion, we found that 14M $Ni_{50}Mn_{25}Ga_{20}Fe_5$ single variant samples showed commensurate modulation with the wave vector expected by the nanotwinned model [37,38] and also recorded in prior research for Ni–Mn–Ga alloys [23–25,47]. In such samples, we observed low TS of 0.1 and 0.2 MPa for both, respectively, type I and type II *a/c* TBs at temperatures over 30° below T_A. Since our preliminary analysis suggests the weaker temperature dependence of TS for type I TB in 14M compared to 10M martensite, the detailed measurement of this dependence is of utmost importance due to its significance for practical applications.

Declaration of Competing Interest

The authors declare that they have no known competing financial interests or personal relationships that could have appeared to influence the work reported in this paper.

Acknowledgment

Authors from Finland were supported by the Strategic Research Council (SRC) of Finland through the grant no. 313349. Authors from Czech Republic were supported by the Ministry of Education, Youth and Sports of the Czech Republic within the program OP VVV Excellent Research Teams under Project CZ.02.1.01/0.0/0.0/15_003/0000487-MATFUN and from the Czech Science Foundation project nr. 17-00062S. RC acknowledges support from the project 2018/29/B/ST8/02343 of the National Science Centre of Poland.

References

[1] O.B.M. Hardouin Duparc, J. Mater. Sci. 52 (2017) 4182.
[2] L. Sun, X. He, J. Lu, Npj Comput. Mater. 4 (1) (2018) 6.
[3] H. Huang, X. Li, Z. Dong, W. Li, S. Huang, D. Meng, X. Lai, T. Liu, S. Zhu, L. Vitos, Acta Mater. 149 (2018) 388.
[4] E. Salje, Ferroelastic Mater. Annu. Rev. Mater. Res. 42 (2012) 1.1–1.19.
[5] R.D. James, K.F. Hane, Acta Mater. 48 (2000) 197–222.
[6] I. Aaltio, A. Sozinov, Y. Ge, K. Ullakko, V.K. Lindroos, S.-P. Hannula, in: S. Hashmi (Ed.), Reference Module in Materials Science and Materials Engineering, Elsevier, Oxford, 2016, pp. 1–14.
[7] A. Likhachev, A. Sozinov, K. Ullakko, Mech. Mater. 38 (2006) 551.
[8] A. Sozinov, N. Lanska, A. Soroka, W. Zou, Appl. Phys. Lett. 102 (2013) 021902.
[9] L. Straka, O. Heczko, H. Seiner, N. Lanska, J. Drahokoupil, A. Soroka, S. Fähler, H. Hänninen, A. Sozinov, Acta Mater. 59 (2011) 7450.
[10] A. Sozinov, N. Lanska, A. Soroka, L. Straka, Appl. Phys. Lett. 99 (2011) 124103.
[11] L. Straka, A. Soroka, H. Seiner, H. Hänninen, A. Sozinov, Scr. Mater. 67 (2012) 25.
[12] O. Heczko, V. Kopecky, A. Sozinov, L. Straka, Appl. Phys. Lett. 103 (2013) 072405.
[13] A. Saren, K. Ullakko, Scr. Mater. 139 (2017) 126.
[14] E. Pagounis, M.J. Szczerba, R. Chulist, M. Laufenberg, Appl. Phys. Lett. 107 (2015) 152407.
[15] S. Guo, Y. Zhang, B. Quan, J. Li, Y. Qi, X. Wang, Smart Mater. Struct. 14 (2005) S236.
[16] D. Soto, F.A. Hernández, H. Flores-Zúñiga, X. Moya, L. Mañosa, A. Planes, S. Aksoy, M. Acet, T. Krenke, Phys. Rev. B 77 (2008) 184103.
[17] Y. Hayasaka, S. Aoto, H. Date, T. Kanomata, X. Xu, R.Y. Umetsu, M. Nagasako, T. Omori, R. Kainuma, T. Sakon, H. Nishihara, K.R.A. Ziebeck, J. Alloys Compd. 591 (2014) 280.
[18] X. Jin, M. Marioni, D. Bono, S.M. Allen, R.C. O'Handley, J. Appl. Phys. 91 (2002) 8222.
[19] Z.-Z. Li, Z.-B. Li, Y.-Q. Yang, Bo Yang, X. Zhao, L. Zuo, Key Eng. Mater. 727 (2017) 244.
[20] C.-M. Li, H.-B. Luo, Q.-M. Hu, R. Yang, B. Johansson, L. Vitos, Phys. Rev. B 84 (2011) 024206.
[21] S.K. Ayila, R. Machavarapu, S. Vummethala, Phys. Stat. Sol. B 249 (2012) 620.
[22] A. Sozinov, A. Likhachev, N. Lanska, O. Söderberg, K. Ullakko, V.K. Lindroos, Mater. Sci. Eng. A 378 (2004) 399.
[23] V.V. Martynov, V.V. Kokorin, J. Phys. III 2 (1992) 739.
[24] V.V. Martynov, J. Phys. IV C 8 (1995) 91.
[25] J. Pons, V.A. Chernenko, R. Santamarta, E. Cesari, Acta Mater. 48 (2000) 3027–3038.
[26] L. Righi, F. Albertini, E. Villa, A. Paoluzi, G. Calestani, V. Chernenko, S. Besseghini, C. Ritter, F. Passaretti, Acta Mater. 56 (2008) 4529.
[27] L. Righi, F. Albertini, A. Paoluzi, S. Fabbrici, E. Villa, G. Calestani, S. Besseghini, Mater. Sci. Forum 635 (2010) 33.
[28] A L. Righi, F. Albertini, S. Fabbrici, A. Paoluzi, in: V.A. Chernenko (Ed.), Advances in Magnetic Shape Memory Materials, 684, Trans Tech Publications Ltd, Zurich, Switzerland, 2011, pp. 105–116.
[29] A. Janner, T. Janssen, Phys. Rev. B 15 (2) (1977) 643.
[30] T. Janssen, A. Janner, A. Looijenga, P.M. Wolff, International Tables for Crystallography, vol. C, Kluwer Academic Publishers, Dordrecht, 1992 Section 9.8.
[31] Z. Li, Y. Zhang, C. Esling, X. Zhao, Y. Wang, L. Zuo, J. Appl. Cryst. 43 (2010) 617.
[32] Z. Li, Y. Zhang, C. Esling, X. Zhao, L. Zuo, Acta Mater. 60 (2012) 6982.
[33] T. Fukuda, H. Kushida, M. Todai, T. Kakeshita, H. Mori, Scr. Mat. 61 (2009) 473.
[34] S.O. Mariager, T. Huber, G. Ingold, Acta Mat. 66 (2014) 192.
[35] S. Singh, V. Petricek, P. Rajput, A.H. Hill, E. Suard, S.R. Barman, D. Pandey, Phys. Rev. B 90 (2014) 014109.
[36] S. Singh, S.R. Barman, D. Pandey, Z. Kristall.-Crys, Mat. 230 (1) (2015) 13.
[37] S. Kaufmann, U.K. Rößler, O. Heczko, M. Wuttig, J. Buschbeck, L. Schultz, S. Fähler, Phys. Rev. Lett. 104 (2010) 145702.
[38] M.E. Gruner, R. Niemann, P. Entel, R. Pentcheva, U.K. Rößler, K. Nielsch, S. Fähler, Sci. Rep. 8 (2018) 8489.
[39] P. Devi, S. Singh, B. Dutta, K. Manna, S.W. D'Souza, Y. Ikeda, E. Suard, V. Petricek, P. Simon, P. Werner, S. Chadhov, S.S.P. Parkin, C. Felser, D. Pandey, Phys. Rev. B 97 (2018) 224102.
[40] H. Seiner, L. Straka, O. Heczko, J. Mech. Phys. Solids 64 (2014) 198.
[41] P. Müllner, Acta Mater. 176 (2019) 211.
[42] J.W. Christian, S. Mahajan, Prog. Mater. Sci. 39 (1995) 1.
[43] J. Wang, H. Sehitoglu, Acta Mater. 61 (2013) 6790.
[44] P. Nnamchi, A. Younes, S. González, Intermetallics 105 (2019) 61.
[45] L. Straka, H. Hänninen, A. Soroka, A. Sozinov, J. Phys: Conf. Ser. 303 (2011) 012079.
[46] R. Chulist, A. Sozinov, L. Straka, N. Lanska, A. Soroka, T. Lippmann, C.-G. Oertel, W. Skrotzki, J. Appl. Phys. 112 (6) (2012) 063517.
[47] A. Sozinov, A. Likhachev, N. Lanska, K. Ullakko, Appl. Phys. Lett. 80 (2002) 1746.